

# CFD characterization of flow regimes inside open cell foam substrates

A. Della Torre<sup>a</sup>, G. Montenegro<sup>a,1,\*</sup>, G. Tabor<sup>b</sup>, L. Wears<sup>b</sup>

<sup>a</sup>*Politecnico di Milano, Department of Energy, via Lambruschini 4, 20156, Milano, Italy*

<sup>b</sup>*College of Engineering, Mathematics and Physical Sciences (CEMPS), University of Exeter, UK*

---

## Abstract

In this work a combination of micro-CT, image-based modelling and CFD has been applied to investigate the pressure drop in open-cell foams. The analysis covers a range of flow regimes and is aimed at determining the effects of important morphological parameters on the pressure drop. The adoption of micro-CT technology and Image Based Meshing allows the investigation of phenomena occurring in real foam micro-structures. Moreover, by means of image processing tools, the geometry can be artificially modified in order to investigate the effects of mathematical transformation of the geometrical parameters of a real foam, one parameter at a time, e.g. varying pore size without affecting the porosity. Non-dimensional coefficients have been defined for the analysis of the results, with the purpose of describing the pressure drop as a function of the Reynolds number. The proposed formulation allows us to relate the permeability properties of an open-cell foam to its morphology alone, without any dependence on the properties of the

---

\*Corresponding author

*Email address:* gianluca.montenegro@polimi.it (G. Montenegro )

<sup>1</sup>phone: +39 0223998639

fluid adopted or on the effective characteristic dimension of the foam microstructure (pore or cell size). Comparison with experimental results available in the literature is also provided for one of the cases studied.

*Keywords:* open-cell foam, pressure drop, CFD, turbulence, pore size, porosity

---

## 1. Introduction

Open-cell foams are cellular materials consisting of a porous matrix of interconnected solid struts delineating numerous multiply connected pseudo-spherical pores, whose interconnections allow the passage of the fluid through the structure. Such foams can be metallic or non-metallic. Their main properties are light weight, high surface to volume ratio and high permeability to the fluid flow, making foams suitable in a wide range of engineering applications. These include structural applications, mechanical energy absorbers, filtering devices and pneumatic silencers [1]. With specific regard to fluid flow and heat transfer applications, foams can be used in the design of compact heat exchangers, heat sinks for cooling of microelectronic devices such as computer chips or power electronics, or as catalytic substrates in exhaust treatment devices for internal combustion engines [2]. For this last application open-cells foams are regarded with interest as a substitute for the traditional honeycomb monolithic substrate: the adoption of a package of foam layers having different properties could lead to a more flexible design for the device, allowing it to deal in a more effective way with the typical requirements such as low pressure drop, high catalytic surface, and fast heating after cold engine start.

The pressure drop given by the foam is one of the key parameters in the design of devices involving porous media. Many works are available in the literature investigating the phenomena leading to the pressure drop, focusing in particular on the influence of the flow regime and on the effects of the geometrical properties.

With regard to the flow regime many authors [3, 4, 5, 6] agree that, in a generic porous media, a transition from laminar to turbulent flow will occur at a critical  $Re$  number. The flow regime occurring in the media for a particular pressure gradient is strictly dependent on the geometrical parameters, the porosity and the pore size. The latter is usually used as the characteristic dimension in the definition of the pore-based  $Re$  number [7]: small pore size usually leads to low  $Re$ , restricting the regime to the laminar range. This is the case for low permeability porous media such as soil, for which the analysis can be reduced to the Darcy-Forchheimer laminar regime. Considering open-cell foams, manufacturing processes can create a wide range of porosities and pore sizes, valuable for different applications. This means that different flow regimes can occur in a foam depending on its geometric parameters. In particular, the flow can become turbulent when high porosity and pore size foams are considered. Several experimental studies have been conducted to assess the validity of the Forchheimer-modified Darcy law beyond the limits of the laminar regime. Experiments on packed-beds and open-cell foams shows a deviation of the pressure drop from the original Darcy-Forchheimer law [8, 9, 10, 11] for these cases.

When an open-cell foam matrix is included in a device, the most important design parameters for the optimization of the foam behaviour are

the geometrical properties and, to some extent, the topology of the micro-structure. This justifies the effort to characterize the dependence of pressure drop on the foam geometrical properties. Several correlations have been proposed in the past to relate the permeability and form coefficient of the foam to the porosity and/or pore size; a complete list of correlations based on empirical and analytical models can be found in [12]. With regard to the topology, this is usually quite standard since open-cell foams are manufactured for most cases with pseudo-spherical cells. However, the topology is often modified a-posteriori by means of compression, in order to enhance heat-transfer properties. Experimental work from Boomsma [13] and Dukhan [14] investigated the effects of compression factor, porosity, and pore size for aluminum foams.

Along with experimental investigations, CFD approaches have been applied to the study of open-cell foams. Two main approaches have been adopted to reproduce the complex micro-structural geometry. Some authors [7, 15] have considered an idealized periodic structure, generated in order to match specific global parameters such as the porosity or the averaged dimensions of pores and struts. The main advantage of this approach is that the computational domain can be reduced to a single elementary cell, which coincides with the Representative Elementary Volume (REV) of the foam. Another approach consists of adopting X-ray computed tomography [16, 12, 36] to record the foam micro-structure, using suitable techniques [17] for the generation of the geometry and computational mesh from the scanned images.

The aim of the present work is to apply CFD to the investigation of the

phenomena affecting the pressure drop in an open-cell foam. CFD is a valuable tool for understanding the physics, since it gives an insight into details of the flow which are difficult to obtain experimentally. In this study the transition from the laminar to the turbulent regime in an idealized foam is investigated by means of unsteady detailed numerical simulations. The effects on the pressure drop are analysed, showing a deviation from the laminar Darcy-Forchheimer standard behaviour. Moreover, a real foam micro-structure was reconstructed by means of computer tomography, in order to investigate the influence of fluid properties, porosity and pore size on the pressure drop.

The paper is structured as follow. Firstly the methodology adopted in this investigation will be explained. Then a brief discussion on the physical models proposed in previous works for the description of the pressure drop in porous media will be given. The problem will be studied resorting to non-dimensional considerations, defining quantities and developing a relationship to be adopted for the analysis of the results. Finally, the CFD model used in this work will be discussed and the results will be presented and analysed, together with comparison with previous studies published in the literature.

## **2. Methodology**

The analysis has been conducted using a combination of micro-CT, image-based modelling and CFD. The first two techniques have been applied to reconstruct the actual geometry of a metallic foam and to generate a computational mesh, on which the CFD simulations were performed. The approach is quite general and can be applied in different fields, some examples can be found in the literature related to biomedical applications [18], simulation of

flow in packed beds [19] or open-cell foams [16]. With regard to simulations of open-cell foams, this technique allows the consideration of the real micro-structure of the media without introducing any idealization of the geometry. Moreover, the reconstructed geometry can be artificially modified in order to investigate the effects of mathematical transformation of the geometric parameters of the foam. Opening or dilation transformations can be applied in order to modify, in an independent way, parameters such as the porosity or the pore size. This kind of study would be difficult experimentally, since it would require the use of different foam samples which could not be guaranteed to have exactly the same morphology. In addition, the effect of parameters such as the specific surface or the cell size distribution have been investigated: these are difficult to be measured experimentally but easy to be determined when the reconstructed geometry is available.

In the first stage of the work an ideal foam structure generated by CAD has been considered. In this case the regular morphology of the foam allows us to exploit some symmetries in the solution of the problem in such a way that the dimension of the representative elementary volume (REV) for the micro-structure is minimized. A detailed unsteady simulation has been set up in order to assess aspects of the flow regimes at different Reynolds numbers. These simulations have been used as points of comparison for steady RANS simulations, in order to obtain guidelines for the choice of the mesh refinement level and of the appropriate turbulence model. Once the proper choice of mesh and turbulence model was determined, RANS simulations were performed on a real foam geometry in order to investigate its permeability properties and the effects of variation of its geometric parameters.

In order to consider flow regimes characterized by a  $Re$  number higher than the upper limit of validity of the Darcy-Forchheimer law, generic non-dimensional coefficients were defined for the analysis of the results.

### 2.1. Ideal foam geometry

Geometric idealizations of the foam micro-structure have been largely adopted for analytical and computational studies [20, 7]. The main advantage of the simulation of an ideal foam is that the regular structure of the geometry together with the application of cyclic boundary conditions allows the reduction of the simulation to a single elementary cell. This leads to a considerable reduction of the size of the problem to solve, resulting in a significant speed-up of the calculations. On the other hand, it becomes also feasible to refine the computational grid, in order to set up a detailed unsteady simulation for investigating the turbulence phenomena occurring at high- $Re$  flow regimes.

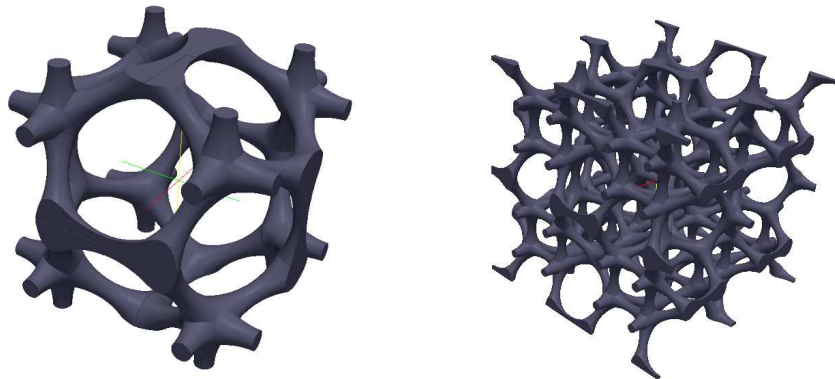


Figure 1: Elementary cell of the ideal foam.

The shape of the elementary cell of the ideal foam was created on the basis of the typical morphology of open-cell foams. These, as pointed out in [21],

generally consist of cells with 12 to 14 pentagonal or hexagonal faces, with ligaments of triangular or cylindrical cross-section and material clustering at the stand vertices. Figure 1 shows the elementary cell created using a CAD tool and the combination of several cells to form a larger foam sample. Once the shape is fixed, the geometry of the elementary cell can be varied acting on its geometrical parameters, for instance the cell dimension, the strut thickness and the radius of the sphere modelling the interconnection between different ligaments. The properties of the ideal foam considered in this work are listed in table 1.

|                                |                     |
|--------------------------------|---------------------|
| porosity [-]                   | 0.903               |
| spec. surf. [ $m^2/m^2$ ]      | 786.4               |
| cell size [ $m$ ]              | $2.1 \cdot 10^{-3}$ |
| strut thickness [ $m$ ]        | $1.5 \cdot 10^{-4}$ |
| interconnection radius [ $m$ ] | $3.5 \cdot 10^{-4}$ |

Table 1: Properties of the ideal foam.

## 2.2. Micro-CT technique

The second step of the analysis was to move towards a real foam structure. To this purpose a sample of a real open-cell Al-alloy foam, having relative density equal to 4% and 40 ppi nominal pore density, was considered in this work (Figure 2). Micro Computed Tomography has been applied for the reconstruction of the actual geometry of the sample. In a micro-CT scanner a X-ray cone beam passes through the sample and is collected by a detector; the sample is rotated providing a series of 2D projection images at different angles. A 3D voxel dataset is then reconstructed from the stack of 2D images

using inverse methods. In the current case a Nikon Metrology Benchtop 160 micro-CT system was used; this uses an electron gun operating at up to 160 keV and a metal target to generate a cone of X-rays through bremsstrahlung; both the electron gun voltage and target metal can be altered to provide a range of spectra and penetration suitable for imaging a range of material compositions from soft biological samples to metal composites, including the metal foams used here. The sample is mounted in the beam between the target and a flat panel detector, and rotated to provide the 2D projection images. The exact resolution depends on the ratio between the target-sample and target-detector distances and is thus dependent on the beam angle and sample dimensions, but resolutions down to  $3\mu m$  are possible. Table 2 summarizes the most significant parameters used for the X-ray scan of the Al foam sample.

|                                  |      |
|----------------------------------|------|
| electron gun voltage [keV]       | 80   |
| electron gun current [ $\mu A$ ] | 95   |
| number of images [-]             | 2500 |
| resolution [ $\mu m$ ]           | 31   |

Table 2: Micro-CT scanner parameters.

The voxel dataset has been segmented using the software ScanIP (Simpleware Ltd). Segmentation is a process of binarisation of the data set into fluid and matrix regions identified as a binary allocation of voxels in the dataset. ScanIP provides numerous tools for the automatic or (where necessary) segmentation of the data, including thresholding algorithms used here. The segmentation process (Figure 3) is not unique because the correct threshold

value on the grayscale of the image for the transition between solid and fluid is not known *a priori*. However, as shown in Figure 4, there is a relationship between the porosity of the reconstructed foam geometry and the threshold value: if the actual porosity of the foam is experimentally measured, this information can be properly used for setting the correct threshold value. At this stage it is also possible to apply various mathematical transformations to the mask, e.g. erosion or dilation, in order to manipulate the mesh geometry; this will be discussed further later in the paper. Having segmented the voxel dataset a base cartesian mesh is then created using the Marching Cubes algorithm which is then truncated and smoothed to form a surface geometry of the microstructure which can be exported as an STL (stereolithography) file.

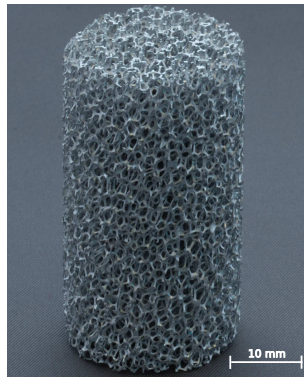


Figure 2: Picture of the Al foam sample.

### 2.3. Mesh generation and geometric characterization

The computational mesh was generated starting from the STL geometry file, generated by CAD or by the segmentation software. For the meshing process a cartesian mesh generator (*snappyHexMesh*, a utility included in

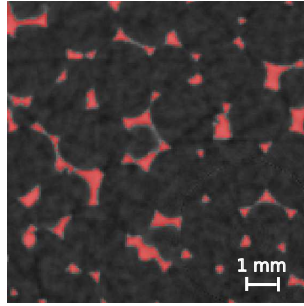


Figure 3: Segmentation of the voxel dataset by means of ScanIP.

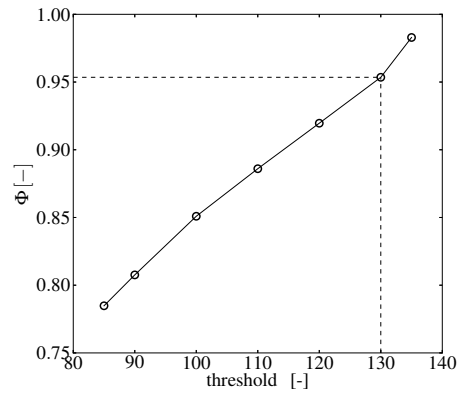


Figure 4: Dependency of the reconstructed foam porosity on the threshold value on the gray-scale.

the open-source CFD toolbox OpenFOAM [22]) was adopted. It is based on the octree concept, where each cell is halved in the proximity of the boundaries. In a first stage, the castellated mesh approximates the shape of the foam in a stair-step way. Then, vertices are moved to the nearest boundaries by means of a smoothing algorithm. Therefore, the mesh generated adopting this strategy is predominantly hexahedral, with a small percentage of polyhedral elements near the boundary walls, as shown in Figure 5. The reconstructed geometry has been characterized in terms of the quanti-

ties defining the geometrical properties of the micro-structure, namely the porosity  $\Phi$ , the specific surface  $\sigma$ , the cell size  $d_c$  and the pore size  $d_p$ . All these quantities have been determined from the computational mesh. In particular the cell and pore sizes were computed on the basis of the opening-size approach adopted by Vogel [23]. This consists of associating at every point in the space the diameter of the largest sphere which includes the point and fits completely within the void space. Then, the implemented algorithm reconstructs the void space with regular spherical elements by flagging the points contained in each sphere by its diameter value, as shown in Figure 6. The plot of the size distribution of the spherical elements (Figure 7) exhibits two distinct maxima, corresponding to the characteristic dimension of the cells and of the pores.

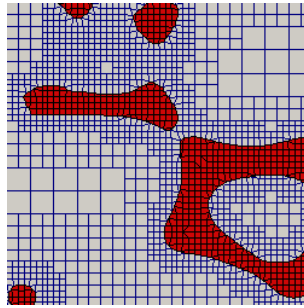


Figure 5: Mesh generated with *snappyHexMesh*.

#### 2.4. Artificial modification of foam geometrical parameters

The geometrical parameters of the AI foam described so far were modified by applying particular mathematical transformations within ScanIP in order to investigate the effect on the pressure drop. The application of mathematical transformations to the geometry allows us to modify the geometric

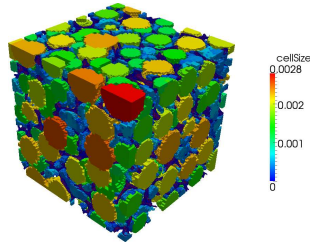


Figure 6: Reconstruction of the void space by means of regular spherical elements.

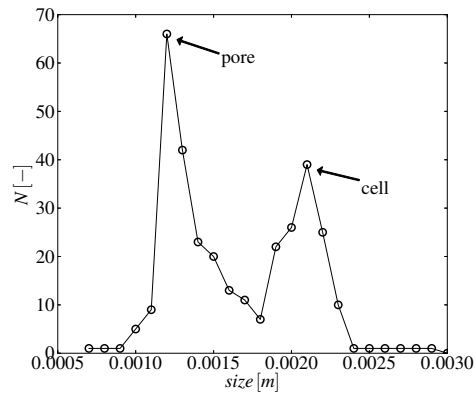


Figure 7: Al foam cell size distribution.

parameters of the micro-structure without affecting its shape, in such a way that similar foam geometries are considered. In this way it is possible to reduce the number of variables involved in the analysis and so clearly distinguish the effects of each parameter.

The first type of transformation consisted of a *dilation* of the geometry in the three dimensions. This allowed the modification of the pore density of the foam (or the cell size) without changing the morphology, the porosity  $\Phi$  or the surface density  $\sigma$ . Three samples with modified pore densities (Figure 8) relative to the original 40 ppi, were considered: 80 ppi, 20 ppi, 10 ppi.

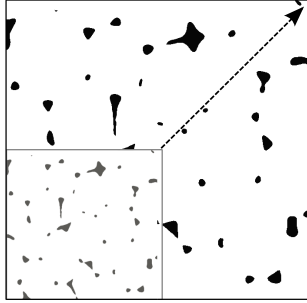


Figure 8: Artificial modification of the pore density: 40 ppi (gray) and 20 ppi (black). Pore density decreases in the direction of the arrow.

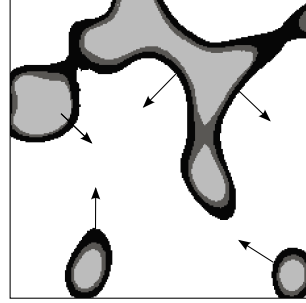


Figure 9: Artificial modification of the porosity: 79%, 86%, 90%. The porosity decreases as the geometric boundary of the foam is moved in the direction of the arrows.

The properties of these foams are listed in Table 3.

|                           | 80 ppi               | 40 ppi               | 20 ppi               | 10 ppi               |
|---------------------------|----------------------|----------------------|----------------------|----------------------|
| porosity [-]              | 0.96                 | 0.96                 | 0.96                 | 0.96                 |
| spec. surf. [ $m^2/m^3$ ] | 1389.0               | 694.5                | 347.3                | 173.6                |
| cell size [ $m$ ]         | $7.35 \cdot 10^{-4}$ | $1.47 \cdot 10^{-3}$ | $2.94 \cdot 10^{-3}$ | $5.88 \cdot 10^{-3}$ |

Table 3: Properties of the foams with different pore density.

The effect of a variation of the porosity was investigated by applying an *opening* transformation on the base real foam: this operation, performed on the voxel dataset, consists of moving, by a certain number of pixels, the boundary of the solid region in a direction normal to the surface (Figure 9). In this way the morphology of the micro-structure is preserved but the actual cross-section of the ligaments constituting the solid matrix is changed. This transformation determines a change of the porosity and the specific surface of the foam, as shown in Table 4.

|                           | 96%                  | 90%                  | 86%                  | 79%                  |
|---------------------------|----------------------|----------------------|----------------------|----------------------|
| porosity [-]              | 0.956                | 0.897                | 0.857                | 0.785                |
| spec. surf. [ $m^2/m^3$ ] | 694.5                | 1033.5               | 1166.2               | 1353.3               |
| cell size [ $m$ ]         | $1.47 \cdot 10^{-3}$ | $1.44 \cdot 10^{-3}$ | $1.42 \cdot 10^{-3}$ | $1.41 \cdot 10^{-3}$ |

Table 4: Properties of the foams with different porosity.

### 3. Physical model

From a literature survey four different flow regimes can be distinguished in a generic porous media: a) Darcy, b) Forchheimer, c) post-Forchheimer and d) Fully-turbulent regime [4, 5, 6, 24]. These can be classified on the basis of the Reynolds number:

$$Re_p = \frac{\rho U L_p}{\mu}, \quad (1)$$

in which  $L_p$  represents a characteristic dimension for the media micro-structure. A possible definition of  $L_p$ , often used in the study of granular media [7] consists of adopting the square root of the permeability  $\sqrt{K}$ , leading to the permeability-based  $Re_K$ . However, a better method for characterizing the flow, especially when open-cell foams are considered, is to use the pore-based  $Re_p$  [13, 25], where the characteristic dimension  $L_p$  is assumed equal to an average pore size. This definition has the advantage of being based only on a foam geometrical dimension and, in contrast to  $Re_K$ , does not depend on the permeability, which needs a direct measurement of the pressure drop in order to be determined. Considering the latter definition of the Reynolds number, limit values can be specified to distinguish between different flow regimes. For  $Re_p < 1$  the Darcy regime occurs: in this regime the flow is dominated

by viscous forces and Darcy’s law, which states that the pressure gradient is directly proportional to the Darcy velocity, holds. The Forchheimer regime occurs for  $1 - 10 < Re_p < 150$ : the flow is dominated by inertial forces and the relationship between pressure gradient and velocity becomes non-linear. The most common model for describing the flow in these two regimes is expressed by the Darcy-Forchheimer relationship:

$$\frac{\Delta p}{L} = \frac{\mu}{K} U_D + \rho C U_D^2. \quad (2)$$

At higher  $Re_p$  the flow becomes unsteady. In particular, for  $150 < Re_p < 300$ , in the post-Forchheimer regime, laminar wake oscillations appear, and, for  $Re_p > 300$ , the flow becomes fully-turbulent, highly unsteady and chaotic. In these regimes the Darcy-Forchheimer law is no longer valid. Different authors have shown significant deviations of the measurements from the Darcy-Forchheimer behavior in the turbulent region. Fand [9] and Kececioglu [10] studied the flow in packed beds and observed that the pressure gradient in the turbulent region correlates with the flow rate in a quadratic fashion, like the Darcy-Forchheimer law, but with different values for the coefficients compared to the laminar Darcy-Forchheimer regime. Deviations from the Darcy-Forchheimer model in the turbulent region were also found by Lage [11], who proposed to correlate the pressure drop by means of a cubic function of the flow speed. Furthermore, experiments on packed beds by Montillet [26] confirm the limits of the validity of the Forchheimer extended Darcy model in the laminar regime, showing that the pressure gradient is no longer a quadratic function of the velocity in the turbulent regime.

In this work CFD has been applied to investigate the pressure drop in an open-cell foam at different regimes. In order to analyze results from the

CFD simulations, comparing cases with different characteristic dimensions or fluid properties, a non-dimensional approach has been adopted to describe the phenomena. The pressure gradient across the foam can be expressed as a function of the quantities that likely have an influence on it:

$$\frac{\Delta p}{L} = f(U_D, \rho, \mu, d_c), \quad (3)$$

where  $U_D$  is the Darcy velocity,  $\rho$  the fluid density,  $\mu$  the fluid viscosity and  $d_c$  a characteristic dimension of the foam micro-structure. By applying the Buckingham- $\Pi$  theorem a relationship in terms of non-dimensional quantities can be derived. If the quantities  $(U_D, \mu, d_c)$  are chosen as repeating variables, Eqn. 3 can be expressed as:

$$\Pi_1 = \frac{\Delta p d_c^2}{L U_D \mu} = \mathcal{F}_1 \left( Re = \frac{\rho U_D d_c}{\mu} \right). \quad (4)$$

If the Darcy-Forchheimer regime is considered, the Darcy-Forchheimer law (Eqn. 2) can be recovered by expressing the functional dependency  $\mathcal{F}_1(Re)$  as:

$$\mathcal{F}_1(Re) = A + B(Re), \quad (5)$$

where:

$$A = \frac{d_c^2}{K}, \quad B = C d_c, \quad (6)$$

where  $K$  is the permeability and  $C$  the form coefficient. In the framework of the Darcy-Forchheimer regime the coefficient  $A$  can be seen as the inverse of an non-dimensional permeability coefficient:

$$K = \frac{d_c^2}{A} = \mathcal{K} d_c^2, \quad \mathcal{K} = \frac{1}{A}. \quad (7)$$

This relation expresses the influence of two contributions on the permeability  $K$ : a non-dimensional permeability  $\mathcal{K}$ , taking into account the morphology

of the foam, and a characteristic dimension of the foam  $d_c$ , expressing the dependency of the pressure drop on the pore size. This suggests, as will be shown in the following, that similar foams having different characteristic dimensions  $d_c$  should behave in a similar way at the same Reynolds number, i.e. they have the same coefficient  $\mathcal{K}$ . In an analogous way, the form coefficient  $C$  is given by two contributions: a non-dimensional form coefficient  $B$  and a characteristic dimension  $d_c$ .

If the analysis is extended beyond the limits of the Forchheimer regime, the Darcy-Forchheimer law can no longer be valid and Eqn. 5 should be replaced with an alternative relationship. In the following it will be shown that the results of CFD calculations can be correlated in the turbulent regime by a similar function to Eqn. 5, but with different values of the coefficients:

$$\mathcal{F}_{1,turb}(Re) = A_{turb} + B_{turb}(Re). \quad (8)$$

This correlation is similar to that proposed in [9, 10] for packed beds. Figure 10 shows the typical dependence of  $\Pi_1$  on the  $Re$  number at the different flow regimes, according to Eqns. 5 and 8.

Moreover an alternative non-dimensional relationship for Eqn. 3 can be derived choosing  $(U_D, \rho, d_c)$  as repeating variables, leading to the following:

$$\Pi_2 = \frac{\Delta p d_c}{L \rho U_D^2} = \mathcal{F}_2 \left( \frac{1}{Re} = \frac{\mu}{\rho U d_c} \right). \quad (9)$$

In this case the coefficient  $\Pi_2$  is related to the Darcy friction factor  $f$  commonly used to describe the pressure drop in circular pipes:

$$\Pi_2 = \frac{1}{2}f. \quad (10)$$

The relationship  $\Pi_2 - Re$ , when plotted in double logarithmic scale (Figure 11), is particularly useful for studying the behaviour at very low Reynolds

numbers, where the  $\Pi_2$  varies as  $A_D/Re$  in the Darcy regime, and at high Reynolds number, where it asymptotes to a constant value  $B_{turb}$  in the fully-turbulent regime.

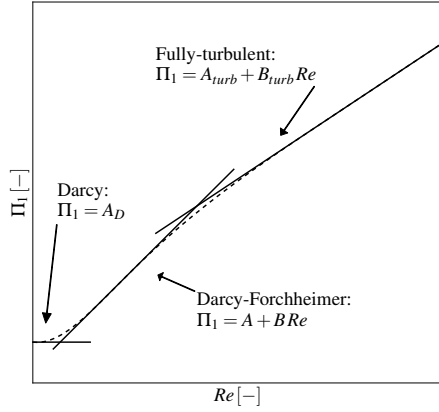


Figure 10: Dependence of  $\Pi_1$  coefficient on  $Re$  number.

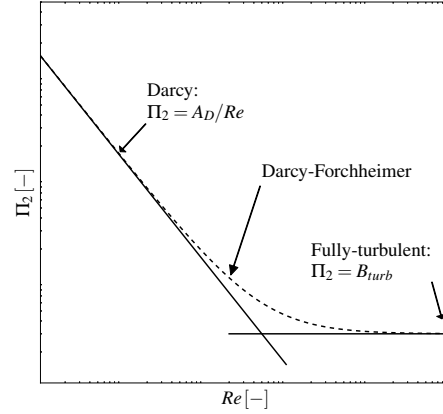


Figure 11: Dependence of  $\Pi_2$  coefficient on  $Re$  number.

#### 4. CFD model

In this work the flow of an incompressible fluid through the micro-structure of open-cell foams was considered. The analysis can also be extended to the case of air because the maximum flow velocity which can be reached in this porous media is usually low, resulting in a Mach number considerably smaller than 0.2, so the flow can be considered incompressible. The governing equations of the flow are the continuity and momentum equations for newtonian

and incompressible flows:

$$\nabla \cdot \mathbf{U} = 0 \quad (11)$$

$$\frac{\partial \rho \mathbf{U}}{\partial t} + \nabla \cdot (\rho \mathbf{U} \mathbf{U}) - \nabla \cdot (\mu \nabla \mathbf{U}) = \nabla p \quad (12)$$

Particularly challenging is the modeling of the flow occurring in the unsteady regimes, post-Forchheimer and fully turbulent. This would be straightforward if it were possible to set up a time-resolved direct numerical simulation (DNS), but this is usually not feasible with the computational capability currently available, especially when the analysis of a large real foam micro-structure sample has to be addressed. However, it becomes an affordable possibility when an ideal regular geometry is considered: in this case the analysis can be focused on a single elementary cell, reducing the size of the problem to solve.

Where it can be applied, DNS provides a detailed description of the flow field considering all the turbulence scales, from the integral scale  $L$  to the Kolmogorov scale  $\eta$ . DNS requires a sufficiently refined grid in order to resolve the smallest dissipative motion. From a theoretical point of view the mesh size should be small enough to model with at least three points the Kolmogorov scale  $\eta$  leading to the  $Re^3$  rule for the estimation of computational effort [27]. However, based on applications reported in literature [35], a ratio 2.1 between the mesh spacing  $\Delta x$  and the Kolmogorov scale  $\eta$  can be regarded as sufficient to guarantee a good accuracy in the solution of the smallest scales. The Navier-Stokes equations are typically solved using high-order schemes, introducing very low numerical dissipation; spectral methods are usually the preferred numerical approaches because of their superior accuracy.

In the case of open-cell foams the integral scale can be assumed to be equal to the cell dimension  $d_c$  and the Kolmogorov length scale can therefore be determined by the following:

$$\eta = d_c Re^{-3/4}. \quad (13)$$

For the estimation of the computational cost of a DNS, it should be considered that in open-cell foams the transition to the turbulent regime occurs at lower Reynolds numbers ( $Re_{p,cr} = 300$ ) compared to other problems, e.g. the flow in pipes ( $Re_{cr} = 2300$ ). This means that the ratio between the integral scale  $L$  and the Kolmogorov scale  $\eta$  at the transition is of the order of magnitude of  $10^2$  (instead of  $10^3$  in the case of pipe), making the simulation of the smallest length scales possible with an acceptable computational burden, i.e. 1 – 10 million cells for the simulation of a single elementary unit of a regular ideal foam.

However in most cases the only way to describe turbulence phenomena in CFD problems is to use a turbulence model. In turbulence modelling, an averaging operation is applied to the Navier-Stokes equations to form an equivalent set of equations for the averaged flow quantities. In the most common approach, an ensemble or Reynolds average is used for this, leading to the Reynolds Averaged Navier Stokes or RANS equations. These are functionally identical to the unaveraged equations but with an additional term present in the momentum equation, the Reynolds Stress term. The averaging process provides a mathematical way to distinguish between deterministic (averaged) and stochastic (turbulent) contributions to the flow, so the Reynolds Stress term represents the effect of the stochastic component of the flow on the mean flow, and can be replaced by a turbulence model

to achieve closure. Since the deterministic component of the flow is much smoother, this means that the solution can be found on a mesh whose element size is several order of magnitude greater than the Kolmogorov length scale: the effects of all the turbulent length scales are taken into account by the turbulence model.

Moreover, when RANS simulation are used, the issue of the modelling of flow behaviour near the wall needs to be considered. In order to have a good quality mesh in the near wall region, a certain level of refinement is usually needed, leading to a value of  $y^+ < 1$ . In this case high-Re turbulence models, such as the  $k - \epsilon$  with standard wall functions, are not suitable and low-Re models should be adopted [27, 28]. These models explicitly solve the flow in the boundary layer, describing the transition from the viscous sublayer to the turbulent core of the flow. However it can be noticed that the complexity of the geometry makes particularly challenging the modelling of the boundary layer with a suitable layered mesh, i.e. hexaedral mesh perpendicular to the surface, and therefore a certain degradation of the quality of the mesh in this region needs to be accepted.

## 5. Numerical Simulations

Numerical simulations were performed using the open-source OpenFOAM CFD software package [29], which is based on the finite volume formulation [30] for the discretization of the governing equations. Simulations were performed first for the ideal foam case and then for the real foam geometry. Two kinds of CFD investigations were performed: direct numerical simulations (DNS) and steady-state laminar/RANS simulations [28].

The DNS, performed only on the ideal foam geometry, was run at two different Reynolds numbers: a)  $Re = 200$ , corresponding to a Post-Forchheimer flow regime, and b)  $Re = 500$  corresponding to a fully turbulent regime. The mesh consists of  $4.1 \cdot 10^6$  elements having size  $\Delta x = 2 \cdot 10^{-5}$ . In Table 5 the Kolmogorov length scale  $\eta$  and temporal scale  $\tau_\eta$  are listed for the two flow regimes. For both cases the mesh size  $\Delta x$  is of the same order of magnitude of the Kolmogorov length scale  $\eta$ , coherently with the aim of describing all the scales of the problem. In Figure 13.a a detail of the mesh is shown: a castellated mesh is adopted to discretize the near-wall region to preserve absolute mesh quality, as against using a body fitted mesh which would require non-orthogonal, non-hexahedral cells, reducing the numerical accuracy.

| $Re$ [-]            | 200                 | 500                 |
|---------------------|---------------------|---------------------|
| $\eta$ [m]          | $1.8 \cdot 10^{-5}$ | $9.4 \cdot 10^{-6}$ |
| $\tau_\eta$ [s]     | $9.0 \cdot 10^{-6}$ | $1.8 \cdot 10^{-6}$ |
| $\Delta x/\eta$ [-] | 1.1                 | 2.1                 |

Table 5: Mesh parameters for the DNS simulations.

The PISO (Pressure-Implicit with Splitting of Operators) algorithm [30] was adopted for the pressure-velocity equation coupling. The convection term in the equations was discretized using a limited third order interpolation scheme (*limitedCubicV* [22], a bounded high-order scheme that takes into account the direction of the flow field). For the discretization of the equation in time the second-order accurate Crank-Nicholson scheme [28] was adopted. The Courant number was set equal to 1 in order to satisfy both accuracy requirement and stability issues.

In order to verify that energy is transferred from large to small scales in a physical way, the turbulent kinetic energy spectrum has been computed. In Figure 12 the spectrum of the turbulent kinetic energy  $E = \frac{1}{2}U_i^2$  is plotted as a function of the product between the wave number  $K = \frac{2\pi f}{U}$  and the Kolmogorov length scale  $\eta$ . It can be seen that, in the inertial subrange, turbulent kinetic energy is transferred from large to small eddies according to the -5/3 law, supporting the validity of the approach.

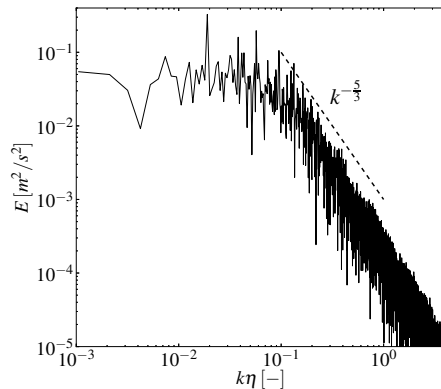


Figure 12: Spectrum of turbulent kinetic energy at  $Re_p = 500$ .

Steady-state laminar/RANS simulations were run for both the ideal and real foams adopting the SIMPLE (Semi-Implicit Method for Pressure Linked Equations) algorithm [31]. The mesh parameters for the discretization were chosen by conducting a sensitivity analysis; the minimum cell size was  $\Delta x = 5.2 \cdot 10^{-4}$  resulting in  $1.2 \cdot 10^6$  cells in the case of the real Al foam. The mesh is refined near the wall up to three times and then snapped on the foam surface, in order to reconstruct the geometry with enough accuracy (Figure 13.b). An upwind scheme was adopted for the discretization of the convective terms. With regards to the turbulence modeling, simulations were run both in the

laminar case or applying the low-Re  $k - \omega SST$  model proposed by Menter [32]. No significant differences were found in the pressure drop prediction between the two cases. Moreover the results were found to be in agreement to those provided by the DNS simulations.

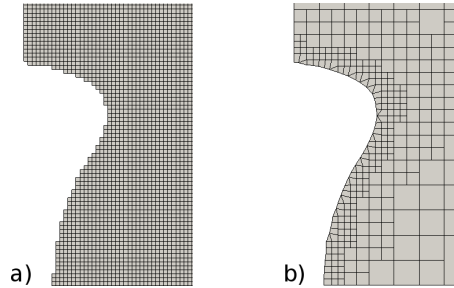


Figure 13: Mesh of a detail of the ideal foam for DNS (a) and RANS (b) simulations.

## 6. Results and discussion

### 6.1. Ideal foam

The computational domain for the ideal foam was created comprising one or more elementary cell units in the direction of the flow, depending on the flow regime. When the analysis is restricted to the laminar regime it is sufficient to consider one single elementary cell for simulating a situation representative of the foam behaviour. This is no longer true when turbulent flow is investigated, since the transition from the laminar to the turbulent regime is completed only after a certain entry length. For this reason an ideal foam composed of only two elementary units will be initially considered for investigating the development of turbulence by means of DNS. The results will be compared with steady-state RANS simulation with different turbulence models. As a second step, domains composed of a higher number of

elementary cells (from 4 to 10) were simulated, investigating the changes in the permeability properties.

Figures 14 - 17 show, for the 2-cell ideal foam, the time-averaged magnitude of the velocity,  $|\overline{\mathbf{U}}|$ , and of the Reynolds stress tensor,  $\rho|\overline{\mathbf{U}'\mathbf{U}'}|$  computed by means of the DNS. The Reynolds stress tensor magnitude provides an indication of the velocity fluctuations. The quantities are calculated for two flow regimes characterized by a  $Re_p$  number of 200 and 500 respectively. It can be noticed that at  $Re_p = 200$ , classified as post-Forchheimer regime in the literature, some instabilities start to appear in the flow, indicating an initial transition of the flow from laminar to turbulent. At  $Re_p = 500$  the velocity fluctuations become more evident as a result of the development of a fully turbulent flow regime.

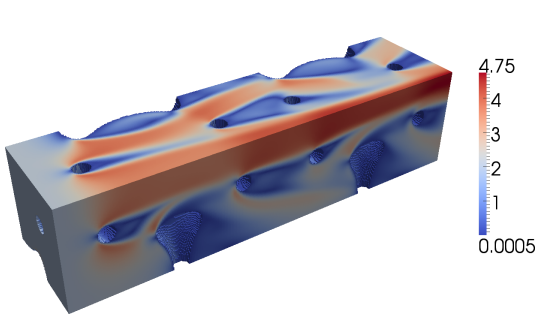


Figure 14: 2-cell ideal foam: time-averaged magnitude of the velocity  $|\overline{\mathbf{U}}|$  at  $Re = 200$

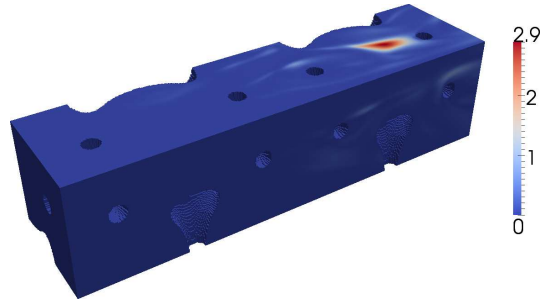


Figure 15: 2-cell ideal foam: time-averaged magnitude of the Reynolds stress tensor  $|\overline{\mathbf{U}'\mathbf{U}'}|$  at  $Re = 200$

In Figure 18 the average pressure on the inlet patch is shown for the two flow regimes as function of the non-dimensional time  $T = t \cdot (U/\Delta x)$  when the steady average condition is reached. It can be observed that the pressure is constant at  $Re_p = 200$ , because turbulence has not yet developed in the

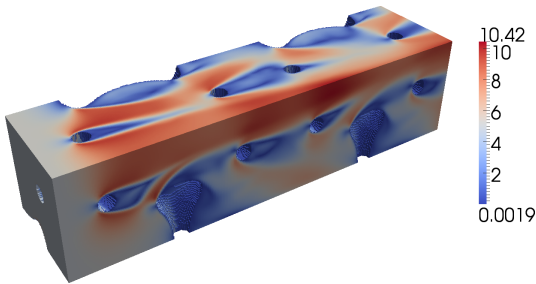


Figure 16: 2-cell ideal foam: time-averaged magnitude of the velocity  $|\overline{\mathbf{U}}|$  at  $Re = 500$

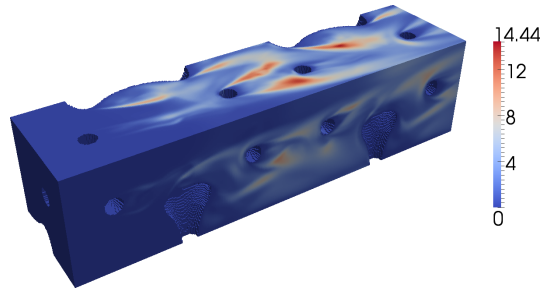


Figure 17: 2-cell ideal foam: time-averaged magnitude of the Reynolds stress tensor  $|\overline{\mathbf{U}'\mathbf{U}'}|$  at  $Re = 500$

flow. On the other hand, at  $Re_p = 500$  the pressure is no longer steady, due to the transition of the flow to the turbulent regime.

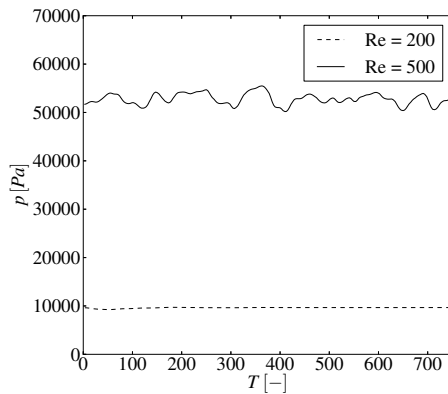


Figure 18: Average of the pressure on the inlet patch as function of the non-dimensional time  $T = t \cdot (U/\Delta x)$ .

Steady-state RANS simulations were run for a wide range of inlet velocities, covering a  $Re_p$  range between 0.1 and 1000. Figure 19 compares the results in terms of pressure gradient  $\Delta p/L$  as function of the Darcy velocity  $U_D$  for three different modeling approaches: a) DNS, b) laminar steady-state

simulation, c) RANS steady-state simulation with a  $k - \omega SST$  turbulence model. It can be seen that these different approaches lead to a similar pressure drop prediction, suggesting that the simulation of the flow through the foam micro-structure can be addressed by use of a simple laminar flow model.

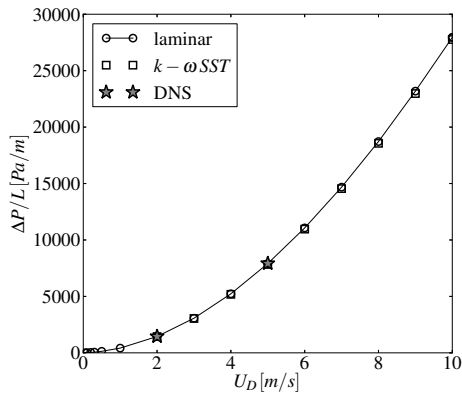


Figure 19: Pressure gradient for the ideal foam.

The results can also be analyzed in terms of the pressure drop coefficients  $\Pi_1$  and  $\Pi_2$  defined in Eqns. 4 and 9. Figure 20 shows the variation of the non-dimensional coefficient  $\Pi_1$  as a function of the  $Re_p$  number. It can be observed that, in the range  $Re = 0 - 150$ , the function exhibits a linear trend: the corresponding Darcy and Forchheimer coefficients can be derived starting from the intercept ( $A$ ) and slope ( $B$ ) of the line.

For Reynolds higher than 150, due to the transition to the turbulent regime, a new trend can be found in the results, with a different intercept and slope of the line if compared to the laminar case. The same conclusions can be drawn considering the  $\Pi_2$  coefficient (Figure 21): a similar change in the slope of the function occurs when passing from the laminar region to the high-Re region. However, for the 2-cell ideal foam the  $\Pi_2$  coefficient does

not asymptote to a constant value at high Reynolds. This behaviour can be explained considering that the flow entering the sample is laminar and the transition to the turbulent flow is completed only after a certain entry length. This portion of sample in which the turbulence is fully-developed increases when the 4-, 8-, 10-cell ideal foams are considered. The plot shows that the solution in the laminar regime is the same for all cases, while different values and trends can be observed in the turbulent region. The function tends to a constant value when the flow is turbulent in a large portion of the sample (8-, 10-cell ideal foams), according to Eqn. 8. On the other hand, when the laminar entry region occupies a large percentage of the sample, as happens for the 4- and 2-cell ideal foams, Eqn. 8 is no longer valid. Moreover, the results do not exhibit significant changes when more than 10 cells are considered, allowing us to conclude that a 10-cell foam is representative of the properties of the media in the turbulent case. The coefficient  $\Pi_1$  for the 10-cell foam case is also plotted in Figure 20, confirming the linear dependency on  $Re$  when the flow becomes fully-turbulent. Finally, considering the plot in Figure 21 and the Moody chart [33] for the flow in a pipe, it can be observed that, in both cases, the pressure drop is a function of  $1/Re$  in the laminar regime and is not dependent on  $Re$  in the turbulent regime.

The velocity field in the foam has been investigated, in order to understand the physical mechanisms affecting the pressure drop in different flow regimes. In Figures 22, 23 and 24 the velocity vectors on two planes normal to the flow direction are shown for both RANS and laminar simulations performed on the 8-cell ideal foam. It can be seen that at  $Re = 5$ , on each plane, the maximum velocity is located where the flow area is the largest (points A1,

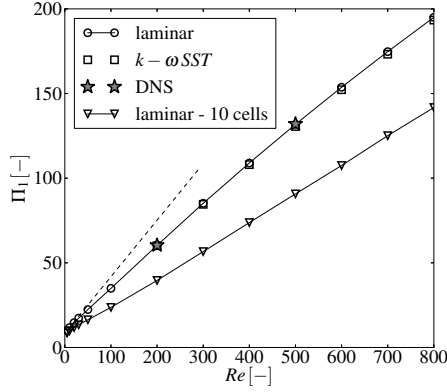


Figure 20: Relationship  $\Pi_1 - Re$  for the ideal foam (2 elementary cells) and for additional case composed with 10 cells. For clarity sake cases with 4 and 8 cells are omitted.

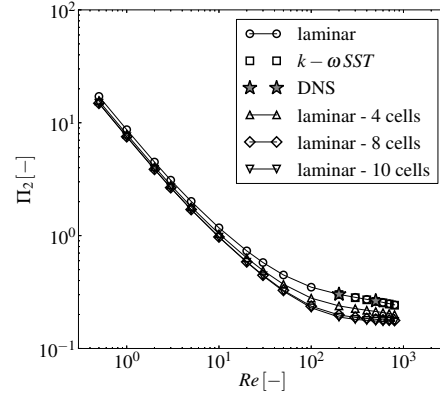


Figure 21: Relationship  $\Pi_2 - Re$  for the base ideal foam (2 elementary cells) and for additional cases composed with 4, 8 and 10 cells.

A2, B3 of Figure 22), while it decreases gradually towards the walls. This behaviour is explained by considering that in the Darcy regime the viscous forces are largely predominant over the inertial forces. At  $Re = 50$ , in the Forchheimer regime, the inertial forces increase, modifying the velocity field distribution. This can be seen on plane B of Figure 23, where the maximum velocity is no longer located at the point B3, which is at the maximum distance from the micro-structure walls on the section considered, but it moves to point B1, which is in the same direction as point A1. On the other hand it is noticeable that the velocity variation from the minimum to the maximum value is gradual, resulting in a parabolic velocity profile, due to the viscous forces which are not negligible. At  $Re = 700$  (Figure 24) the flow is dominated by inertial forces which distort the velocity profile. The maximum

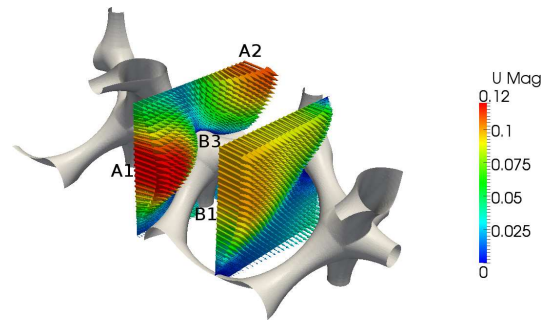


Figure 22: Velocity field in the ideal foam (10-cells) for  $Re = 5$ . Results are visualized in the last cells.

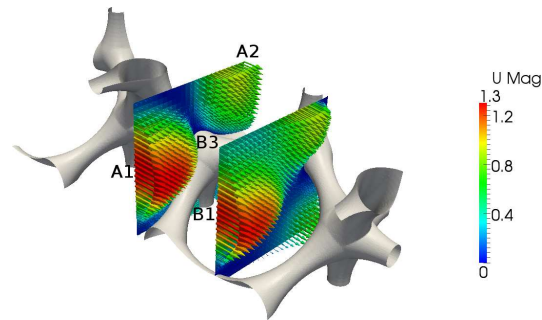


Figure 23: Velocity field in the ideal foam (10-cells) for  $Re = 50$ . Results are visualized in the last cells.

velocity is not located in the middle of the the cross-sectional area open to the flow, as already noted for the Forchheimer regime. Moreover, the viscous forces become negligible compared to the inertial forces, as can be evinced by examining the velocity profile, which shows high gradients passing from the stagnation zones, where velocity approaches to zero, to the flow zones, which are characterized by a nearly constant velocity value.

In a porous medium, two major contributions to the pressure drop can be distinguished, namely viscous and inertial, according to the basic idea expressed by the Darcy-Forchheimer law. Considering the case for  $Re = 5$

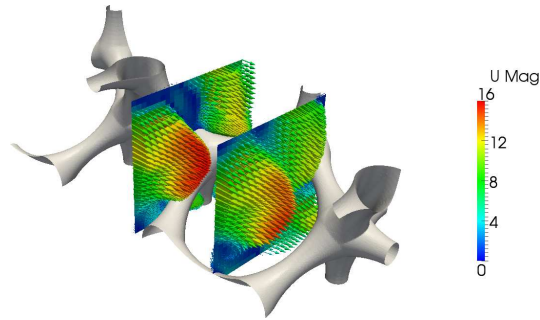


Figure 24: Velocity field in the ideal foam (10-cells) for  $Re = 700$ . Results are visualized in the last cells.

(Darcy regime), it can be noted that the dissipative viscous mechanism is similar to that observed for a laminar flow in a channel, with a variation of the velocity from zero at the wall to a maximum value where the flow area is largest, according to a parabolic profile. At  $Re = 50$  (Forchheimer regime) the flow is still laminar, but the velocity drops to zero not only at the walls but also in stagnation regions occurring within the velocity field. In this regime, due to the effects of inertia, the flow field is modified in such a way that laminar viscous stresses increase. At  $Re = 700$  (fully-turbulent regime) flow regions and stagnation regions can be clearly distinguished. The velocity profile in flow regions exhibits similarities to the turbulent flow in a channel, with a constant velocity value in the bulk of the flow. In the case of open-cell foams this velocity profile is promoted by the mixing of different high inertia flow streams coming from adjacent pores. The dissipation mechanism is related to the high stresses generated at the boundary between stagnation region and flow region, due to the sharp variation in the velocity value.

From this it can be observed that the dissipation mechanism changes significantly at low Reynolds number, due to the increase of inertial forces pass-

ing from Darcy to Forchheimer regimes, and then tends to stabilize when the flow, completely inertia-dominated, becomes fully turbulent. On the other hand, the inertial contribution to the pressure drop (form drag), which is related to the changes in the direction of the flow stream due to the presence of the solid matrix, increases linearly with the flow velocity. The superposition of the two contributions determines the effective dependence of the pressure drop on the  $Re$  number. In particular, it results in two different relationships between  $\Pi_1$  and  $Re$  in the Darcy-Forchheimer and in the fully-turbulent regimes, due to the specific contribution of viscous dissipation and inertial forces.

Despite the fact that turbulence should increase the dissipative contribution to the pressure drop, no significant differences have been demonstrated by means of the approaches previously discussed, namely DNS and RANS simulations with and without turbulence model. The justification of this behaviour is that the major contribution to the pressure drop in fully-turbulent region is given by the high inertial forces in the fluid flow, which are also responsible for the development of turbulence. In this framework, the contribution of turbulence to the dissipation results in a negligible influence on the overall pressure drop, which instead is mainly governed by inertia. In order to support this explanation, the relative contribution of the viscous and inertia forces has been evaluated for the case in exam. In Figure 25 it can be seen that the viscous drag contributes for more than the 50% in the laminar regime, while at high Reynolds numbers its contribution becomes lower than the 25%. In this conditions the pressure drop is mainly determined by the form drag, whereas the contribution of the turbulence, which basically

modifies the quota of the viscous forces, becomes negligible if compared to the overall pressure drop. The large contribution of the inertial forces to the pressure drop represents the main aspect which differentiate the flow in a pipe from the flow through an open-cell foam. Inside a pipe, there is not a form drag contribution and the pressure drop results entirely from the shear stress at the wall. In this case the turbulence plays a key role since it affects the velocity profile and its correct description is mandatory for an accurate prediction of the flow characteristics. On the contrary, in a foam, at high Reynolds, the wall shear stress becomes a secondary factor, while the form drag, which is not affected by the turbulence, gives the major contribution to the pressure drop. In this last case, even if the flow is turbulent, also a laminar model is able to give a sufficiently accurate prediction of the pressure drop.

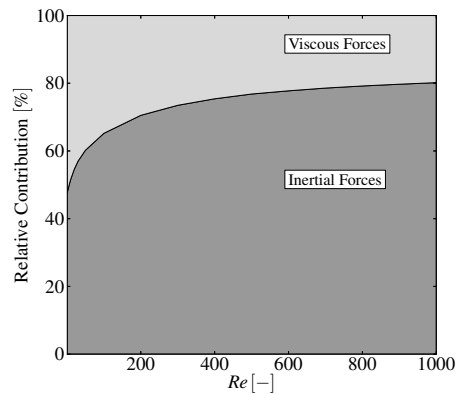


Figure 25: Relative contribution of the viscous and inertial forces as function of the Reynolds number.

## 6.2. Al foam

Steady-state simulations for the Al-foam were run for the laminar case. The analysis aims to investigate how the foam micro-structural properties, like pore density and porosity, influence the pressure drop.

### 6.2.1. Effect of the variation of the pore density

In this section the effect of the modification of the foam pore density is investigated. As shown in Figure 26 the pressure gradient decreases when high pore densities are considered. A plot of the results in terms of  $\Pi_1$  and  $\Pi_2$  coefficients (Figures 27 and 28) shows that the relationship with the  $Re_p$  number is the same for all the different pore densities. In fact the quantities involved, as defined in Eqns. 4, 9, are non-dimensional and therefore the relationship does not vary if the characteristic dimension of the micro-structure is changed. In this case the morphology of the foam was preserved, whereas the characteristic dimension (pore size  $d_c$ ) was changed by applying an artificial transformation of the CAD geometry. Moreover, the same trends highlighted in the case of the ideal foam can also be observed for the real foam: the non-dimensional coefficient  $\Pi_1$  depends on  $Re_p$  in a linear fashion in both the laminar and turbulent regime, but the intercept and the slope change when the transition from laminar to turbulent flow occurs. The coefficients  $A$  and  $B$ , the permeability  $K$  and the form coefficient  $C$ , related to the different pore densities, are listed in Table 6. This analysis suggests that the permeability  $K$  correlates with the pore size  $d_c$  according to the following equation:

$$K = \mathcal{K} d_c^2 = \frac{d_c^2}{A}. \quad (14)$$

This is consistent with the non-dimensional analysis and highlights the fact that the permeability becomes null when the pore size approaches zero. Moreover, the reason for the relationship between permeability and pore size can be found considering that, keeping constant the morphology of the foam, the pore size  $d_c$  is proportional to  $1/\sigma$ . This means that the specific surface decreases with the pore size, reducing the contribution of the viscous forces to the pressure drop. With regards to the form coefficient, it can be found that:

$$C = \frac{B}{d_c}. \quad (15)$$

This means that, for a given foam geometry, the pressure drop due to the inertial term decreases for higher values of the pore size  $d_c$ . In Figure 28 non-dimensional curves of two experimental results published by Du Plessis [34] are also plotted. These are relative to foams having porosity (97%) similar to that one of the Al foam and 45 ppi and 60 ppi pore density. The experimental data seems to be in agreement with the simulations, confirming the validity of the numerical approach.

### 6.2.2. *Effect of the variation of the porosity*

Variation of the porosity cannot be accomplished without affecting the morphology of the foam. When the *opening* operation is performed the pore size and the specific surface of the foam change together with the porosity. This affects both the viscous and inertial contribution to the pressure drop. Figure 29 shows how the pressure gradient increases when the porosity is lowered. Experimental results obtained by Boomsma [13] for a foam having 92% porosity and 40 ppi pore density are also plotted on this graph. This

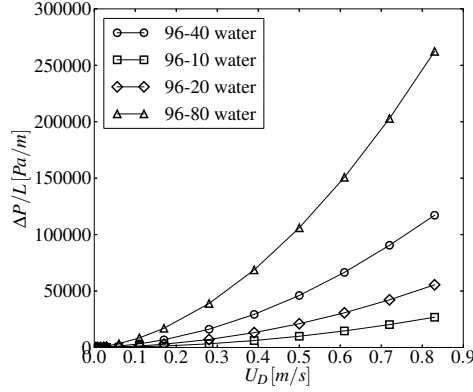


Figure 26: Pressure gradient with different pore densities.

result compares quite well with the calculations on the 90% artificially modified foam. Although the morphology of the foams is different and the two cases are not directly comparable, the similarity in terms of trend and value of the pressure drop supports the validity of the numerical approach. The relationship between the  $\Pi_1$  and  $\Pi_2$  coefficients and the  $Re$  number plotted in Figures 30 and 31 shows the same trend described in the previous sections, with high values of the coefficients for the low porosities. In Table 6 the values of the coefficients in the Darcy-Forchheimer regime and in the turbulent regime are listed.

Furthermore, the dependency of these coefficients on the geometric properties of the foam was investigated. Figure 32 and Figure 33 show that the non-dimensional permeability  $\mathcal{K}$  correlates exponentially with the porosity while the non-dimensional form coefficient  $B$  decreases in a linear fashion. This is in accordance with the experimental work on compressed foam published by Dukham [14], who highlighted the same trends for the permeability and the form coefficient. In order to understand the physical reasons leading

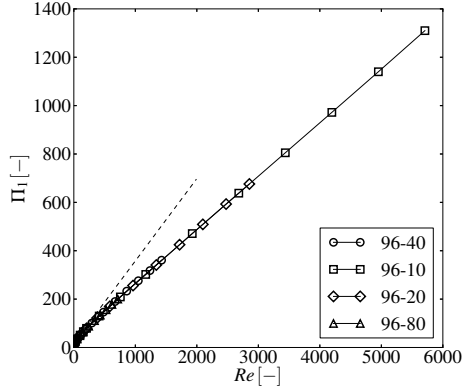


Figure 27: Relationship  $\Pi_1 - Re$  with different pore densities.

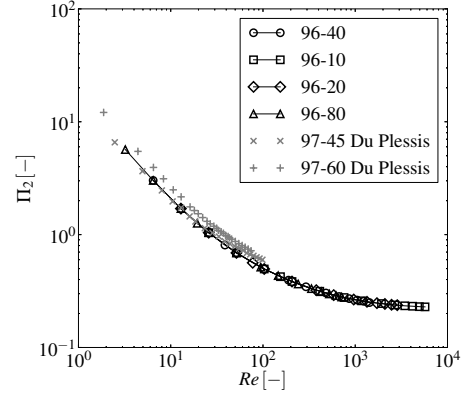


Figure 28: Relationship  $\Pi_2 - Re$  with different pore densities.

to the variation in permeability, the dependency of the surface density on the porosity must be considered. Figure 32 shows a decreasing trend for the surface density, which follows a  $a_1(1 - \exp(a_2\Phi))$  law. This suggests that, considering a porosity variation, the permeability increase is strictly related to the decrease of surface density. This dependency is highlighted in Figure 34, which shows that a linear relationship can be found between the square root of the non-dimensional permeability  $\sqrt{\mathcal{K}}$  and the surface density  $\sigma$ .

The same analysis of the coefficients can be undertaken for turbulent  $Re$  numbers. In these cases the coefficients  $\mathcal{K}_{turb}$  and  $B_{turb}$  can be defined starting from the intercept and the slope coefficient of the trend line in the turbulent region. Figures 32, 33 and 34 show the dependence of  $\mathcal{K}_{turb}$  and  $B_{turb}$  on the geometric parameters. In particular, the same linear dependency on  $\sigma$  and  $\Phi$  highlighted for the low  $Re$  coefficients can be noted also for  $\mathcal{K}_{turb}$  and  $B_{turb}$ . However the value of  $\mathcal{K}_{turb}$  is lower than  $\mathcal{K}$  over the whole range of porosity/specific surface. The same consideration is valid also for  $B_{turb}$ ,

which decreases linearly with the porosity  $\Phi$ , exhibiting however a less steep slope compared to the coefficient  $B$  in the laminar region.

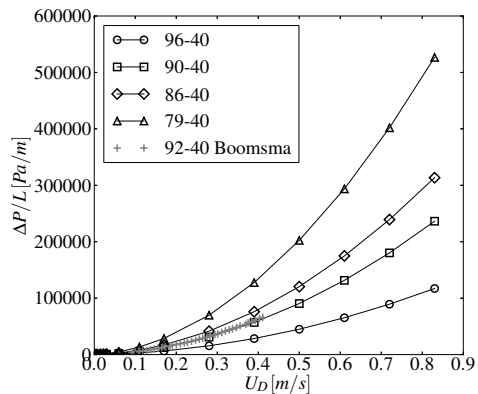


Figure 29: Pressure gradient with different porosities.

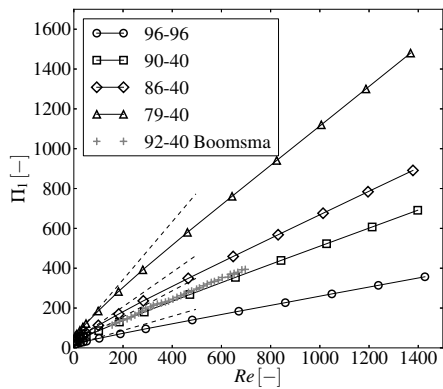


Figure 30: Relationship  $\Pi_1 - Re$  with different porosity.

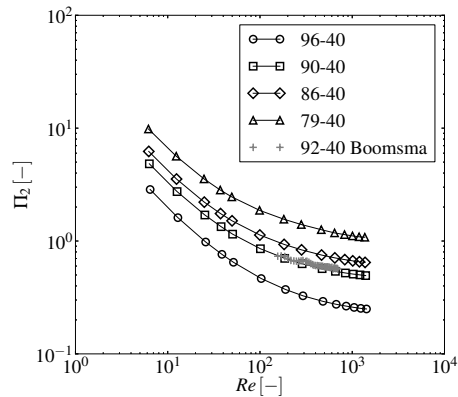


Figure 31: Relationship  $\Pi_2 - Re$  with different porosity.

|             | $A[-]$ | $B[-]$ | $K[10^8 m^2]$ | $C[10^{-2} m^{-1}]$ | $A_{turb}[-]$ | $B_{turb}[-]$ |
|-------------|--------|--------|---------------|---------------------|---------------|---------------|
| 96% – 40ppi | 24.26  | 0.23   | 8.91          | 1.56                | 29.5          | 0.22          |
| 96% – 10ppi | 24.26  | 0.23   | 143.52        | 1.56                | 29.5          | 0.22          |
| 96% – 20ppi | 24.26  | 0.23   | 35.63         | 1.56                | 29.5          | 0.22          |
| 96% – 80ppi | 24.26  | 0.23   | 2.23          | 1.56                | 29.5          | 0.22          |
| 79% – 40ppi | 92.7   | 1.04   | 2.14          | 7.38                | 132.23        | 0.98          |
| 86% – 40ppi | 57.03  | 0.65   | 3.54          | 4.58                | 85.15         | 0.61          |
| 90% – 40ppi | 43.4   | 0.47   | 4.78          | 3.26                | 57.25         | 0.45          |

Table 6: Coefficients computed for the base foam and the artificially modified foams.

## 7. Conclusions

In this work CFD was applied to investigate the physical phenomena affecting the pressure drop in open-cell foams. The study has been based on both ideal and real micro-structures. A detailed unsteady numerical simulation of the flow through an idealized foam micro-structure was used to investigate the transition from laminar to turbulent flow regimes; the results of these preliminary simulations have been used as a basis for comparison of the results obtained with a steady-state RANS approach. The results, analysed in terms of non-dimensional coefficients, were found to be in agreement with previous experimental results on packed beds, showing that the transition from laminar to turbulent regime influences the correlation between pressure drop and Darcy velocity. In particular, although the variation of pressure gradient coefficient with the Reynolds number is quadratic in both the laminar Darcy-Forchheimer regime and the fully turbulent regime, the parameters of the relation change during the transition. The variation of the

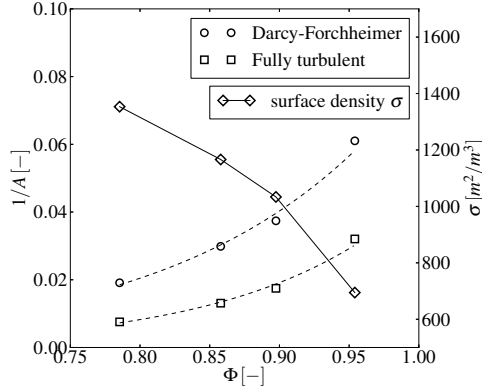


Figure 32: Dependence of  $\mathcal{K}$  and on  $\sigma$  on the porosity  $\Phi$ .

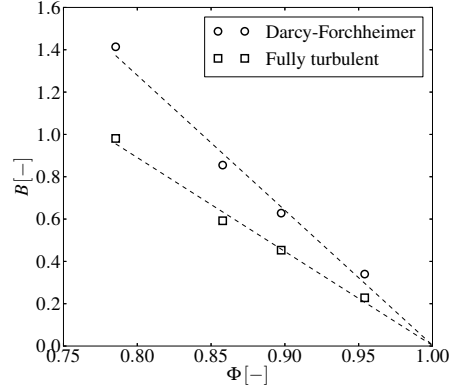


Figure 33: Dependence of  $B$  on the porosity  $\Phi$ .

velocity profiles with the flow regimes has been analysed in order to qualitatively investigate the contribution of viscous and inertial forces to the overall pressure drop.

As a further step, micro-CT and Image Based Meshing techniques were applied in order to study a real foam micro-structure. Steady-state RANS simulations were run, confirming the same trends of the pressure drop coefficients highlighted in the ideal foam case. Mathematical transformations were then applied in order to modify the geometry of the original foam and the effects of the variation of geometrical parameters like porosity and pore size were investigated. It was shown that a pore size reduction determines an increase of the pressure gradient across the sample; however the relationship between pressure gradient and velocity, if expressed in terms of non-dimensional quantities, is unique for all the foams having different pore size but the same morphology. Moreover the results for different fluids are the same when expressed in terms of non-dimensional relationships, allowing

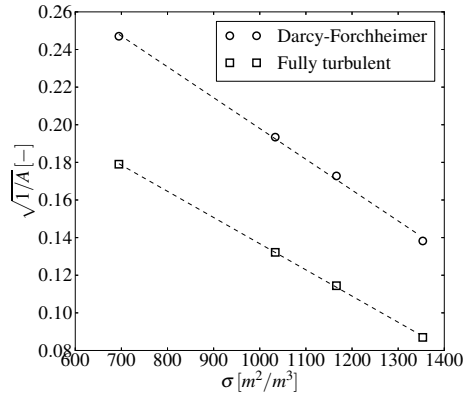


Figure 34: Dependence of  $\sqrt{K}$  on specific surface  $\sigma$ .

the characterization of the flow behaviour for an arbitrary fluid. Finally the effect of variation in the porosity was considered, showing that the dependence of the permeability on the porosity can be assumed to be exponential, as proposed in previous work. The reasons for this behaviour were investigated, leading to the conclusion that the square root of the permeability has a linear dependence on the specific surface, which changes with the porosity following an exponential law.

## References

- [1] John Banhart. Manufacture, characterisation and application of cellular metals and metal foams. Progress in Materials Science, 46(6):559 – 632, 2001.
- [2] Enrico Bianchi, Tobias Heidig, Carlo Giorgio Visconti, Gianpiero Groppi, Hannsjrg Freund, and Enrico Tronconi. An appraisal of the heat transfer properties of metallic open-cell foams for strongly exo-/endo-

- thermic catalytic processes in tubular reactors. Chemical Engineering Journal, 198199(0):512 – 528, 2012.
- [3] D Seguin, A Montillet, and J Comiti. Experimental characterisation of flow regimes in various porous media i: Limit of laminar flow regime. Chemical Engineering Science, 53(21):3751 – 3761, 1998.
- [4] D Seguin, A Montillet, J Comiti, and F Huet. Experimental characterization of flow regimes in various porous media ii: Transition to turbulent regime. Chemical Engineering Science, 53(22):3897 – 3909, 1998.
- [5] D. B. Ingham and I. Pop. Transport in Porous Media II. Pergamon, 2002.
- [6] M. J. S. de Lemos. Turbulence in Porous Media - Modeling and Applications. Elsevier, 2006.
- [7] K. Boomsma, D. Poulikakos, and Y. Ventikos. Simulations of flow through open cell metal foams using an idealized periodic cell structure. International Journal of Heat and Fluid Flow, 24(6):825–834, 2003.
- [8] A. Montillet, E. Akkari, and J. Comiti. About a correlating equation for predicting pressure drops through packed beds of spheres in a large range of Reynolds numbers. Chemical Engineering & Processing, Vol. 46:329–333, 2007.
- [9] R. M. Fand, B. Y. K. Kim, A. C. C. Lam, and R. T. Phan. Resistance to the Flow of Fluids Through Simple and Complex Porous Media Whose Matrices Are Composed of Randomly Packed Spheres. Journal of Fluid Engineering, Vol. 109:268–273, 1987.

- [10] I. Kececioglu and Y. Jiang. Flow Through Porous Media of Packed Spheres Saturated With Water. Journal of Fluid Engineering, Vol. 116:164–170, 1994.
- [11] J. L. Lage, B. V. Antohe, and D. A. Nield. Two Types of Nonlinear Pressure-Drop Versus Flow-Rate Relation Observed for Saturated Porous Media. Journal of Fluid Engineering, Vol. 119:700–706, 1997.
- [12] J. Petrasch, F. Meier, H. Friess, and A. Steinfeld. Tomography based determination of permeability, DupuitForchheimer coefficient, and interfacial heat transfer coefficient in reticulate porous ceramics. Mechanics of Materials, Vol. 29:315326, 2008.
- [13] K. Boomsma and D. Poulikakos. The Effects of Compression and Pore Size Variations on the Liquid Flow Characteristics in Metal Foams. Journal of Fluid Engineering, Vol. 124:263–272, 2002.
- [14] N. Dukhan. Correlations for the pressure drop for flow through metal foam. Experiments in Fluids, Vol. 41:665672, 2006.
- [15] S. Krishnan, Murthy J. Y., and S. V. Garimella. Direct Simulation of Transport in Open-Cell Metal Foam. Journal of Heat Transfer, 128:793–799, 2006.
- [16] G. Tabor, O. Yeo, P. Young, and P. Laity. CFD Simulation of Flow through an Open Cell Foam. International Journal of Modern Physics, Vol. 19:703–715, 2008.
- [17] P. Young, T. B. H. Beresford-West, S. R. L. Coward, B. Notarberardino,

- B. Walker, and A. Abdul-Aziz. An efficient approach to converting computational models three-dimensional image data into highly accurate computational models. Philosophical Transaction of The Royal Society A, Vol. 366:3155–3173, 2008.
- [18] B. Notarberardino, P. G. Young, G. R. Tabor, L. Hao, I. G. Turner, and A. Harkara. Structural and Fluid Transport Characterization of Bio-scaffolds based on 3D Imaging Data. International conference on Biomedical and Pharmaceutical Engineering, 2009.
- [19] M. J. Baker, P. G. Young, and G. R. Tabor. Image based meshing of packed beds of cylinders at low aspect ratios using 3d MRI coupled with computational fluid dynamics. Computers and Chemical Engineering, Vol. 35(No. 10):1969–1977, 2011.
- [20] G. N. Dul’nev. Heat transfer through solid disperse systems. Journal of Engineering Physics and Thermophysics, 9(No. 3):275–279, 1965.
- [21] L.J. Gibson and M.F. Ashby. Cellular Solids. Cambridge University Press, Cambridge, UK, 1997.
- [22] OpenFOAM documentation. Avaiable from:  
<http://www.openfoam.org/docs/>.
- [23] H. J. Vogel. Morphological determination of pore connectivity as a function of pore size using serial sections. European Journal of Soil Science, 48:365–377, 1997.
- [24] K. Vafai. Handbook of porous media. Marcel Dekker, Inc, New York, USA, 2005.

- [25] B. V. Antohe, J. L. Lage, D. C. Price, and R. M. Weber. Experimental determination of permeability and inertia coefficients of mechanically compressed aluminum porous matrices. Journal of Fluids Engineering, 119:404–412, 1997.
- [26] A. Montillet. Flow Through a Finite Packed Bed of Spheres: A Note on the Limit of Applicability of the Forchheimer-Type Equation. Journal of Fluid Engineering, Vol. 126:139–143, 2004.
- [27] C. Hirsch. Numerical Computation of Internal and External Flows: the fundamentals of computational fluid dynamics. Butterworth-Heinemann, 2007.
- [28] J. H. Ferziger and M. Perić. Computational methods for fluid dynamics. Springer, 1997.
- [29] H. G. Weller, G. Tabor, H. Jasak, and C. Fureby. A Tensorial Approach to CFD using Object Orientated Techniques. Computers in Physics, Vol. 12(No. 6):620, 1998.
- [30] H. K. Versteeg and W. Malalasekera. An introduction to computational fluid dynamics. Longman Scientific & Technical, 1995.
- [31] S. V. Patankar. Numerical Heat Transfer and Fluid Flow. CRC Press, 1980.
- [32] F. Menter and T. Esch. Elements of Industrial Heat Transfer Prediction. 16th Brazilian Congress of Mechanical Engineering (COBEM), 2001.

- [33] L. F. Moody. Friction factors for pipe flow. Transactions of the ASME, 66(No. 8):671684, 1944.
- [34] P. Du Plessis, A. Montillet, J. Comiti, and J. Legrand. Pressure drop prediction for flow through high porosity metallic foams. Chemical Engineering Science, 40(No. 21):3545-3553, 1994.
- [35] S. B. Pope. Turbulent Flows. Cambridge University Press, 2000.
- [36] E. Bianchi, T. Heidig, C. G. Visconti, G. Groppi, H. Freund, and E. Tronconi. Heat transfer properties of metal foam supports for structured catalysts: Wall heat transfer coefficient. Catalysis Today, 216(No. 0):121-134, 2013.